Simulation-based Analysis of a Microstructuring Process for Serrated Surfaces with Higher Friction

I. Schaarschmidt[1], P. Steinert[1], M. Hackert-Oschätzchen[1], G. Meichsner[2], M. Zinecker[1], A. Schubert[1,2]
[1]Professorship Micromanufacturing Technology, Chemnitz University of Technology, 09107 Chemnitz, Germany
[2]Fraunhofer Institute for Machine Tools and Forming Technology, 09126 Chemnitz, Germany

Keywords:
Electrical discharge machining, crater formation, surface topography

Introduction

Actual trends in lightweight construction and safety-relevant technologies cause an increasing demand for reliable design of joining connections. Increasing power density and compact design require dimensioning of joints with low safety factors. Thereby additional security measures are needed more often. One possible measure is increasing the friction coefficient of serrated fasteners by microstructuring the serrated surface. Aim of the microstructuring is the development of serrated fasteners with higher breakaway torque. Several studies showed the potential of microstructured surfaces to increase the friction coefficient of two contact surfaces. One possible solution approach is to integrate the microstructuring of the serrated fastener in the conventional machining process chain. Therefore, the forming tools e.g. carbide metal dies need to have the negative geometry of the microstructure. A technology to manufacture such microstructured carbide metal dies is electrical discharge machining (EDM).
EDM is an ablating technology which allows the manufacturing of complex geometries in combination with good surface qualities independent of the hardness of the material. Basic principle of the EDM process is material removal due to thermal impact of a short single discharge. The formation of complex geometries was realized by numerous superimposed single craters. Figure 1 shows the principle of the generation of one single discharge.

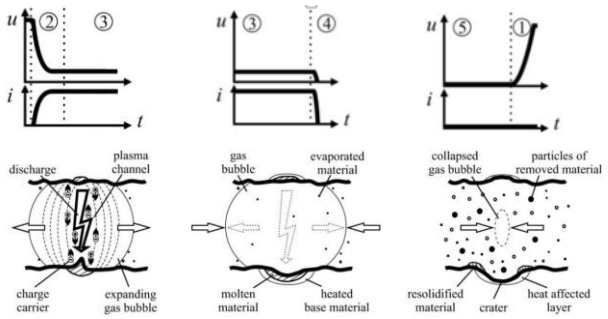

Figure 1. Phenomenological model of a single discharge: (2) Formation of the plasma channel, decrease of the electric voltage, increase of the electric current; (3) Expansion of the plasma channel, electric voltage and electric current almost constant; (4) Collapse of the plasma channel, drop of the voltage and current [1]

The dielectric fluid, which is mostly dielectric oil or deionized water, separates the workpiece and the tool. Between the tool and the workpiece, an electric potential is applied. When the electric field is stronger than the dielectric strength of the dielectric fluid, a discharge appears and a plasma channel is generated. The plasma channel causes a high input of thermal energy into the workpiece and the tool material. Simultaneously the voltage drops to the level of the discharge voltage and the electric current increases. Then voltage and current are almost constant, the plasma channel expands and the workpiece material begins to melt and to vaporize. These phenomena result in a crater formation. After that, the plasma channel and the surrounding gas bubble collapse, when the electric voltage and current are dropped to zero and the molten material is partially ejected. Some of the molten material resolidifies on top of the workpiece surface and forms a bulk at the edge of the crater. In addition a heat-effected layer in the subsurface of the workpiece material occurs.
Several studies have been conducted on analytic and numerical models to describe the heating process due to the single discharge and the mechanism of the following single crater formation.[2–7] Mostly the spark respectively the plasma channel is modelled as a heat source defined as a Gaussian distribution which varies in time and space.[8–12] A small number of the

studies focuses on the modeling of the crater formation with a topology change of the surface. [13, 14]
Within this study a method to simulate a resulting workpiece surface based on a multiphysics simulation of a single crater formation is shown. The ablation process is simulated using the level-set method, which tracks the interface between the dielectric medium and the workpiece surface. Several phenomena are considered to model the resulting crater geometry. The interaction between the plasma channel and the workpiece material leads to a fast heating of the interaction zone and is considered through an additional heat source at the workpiece surface. The heat source is a function of the discharge time and the plasma radius. In consequence, the solid workpiece material is heated and reaches the vaporization temperature. Hence the material removal occurs. A simultaneous phenomenon is the interaction between the vaporization pressure and the molten workpiece, which leads to a flow of the molten material to the outer area of the removal geometry. Based on the resulting crater geometry, a method to calculate the resulting workpiece surface formation is described and analyzed.

Geometry and material parameters for single crater formation with electrical discharge machining

To perform a simulation of the single crater formation a two dimensional axial symmetric geometry was defined which is shown in figure 2. The radius r of the geometry is 80 µm and the height h is 90 µm. The geometry consists of two domains, the dielectric fluid (blue) and the workpiece (grey).

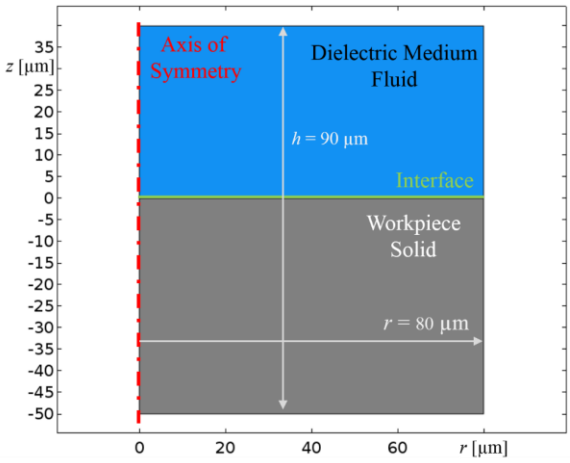

Figure 2. Two-dimensional axial-symmetric geometry

In this work, deionized water was defined as the dielectric fluid. The workpiece material was defined as carbide metal G55. Both materials are assumed as homogenous, isotropic and incompressible. The deionized water as well as the workpiece material were defined as Newtonian fluids, so their viscosities are independent of the shear rate. Furthermore the material properties of the dielectric fluid were assumed independent from temperature and pressure. Table 1 summarizes the material properties of the dielectric fluid and the workpiece material.

Table 1. Material properties of the dielectric fluid and the workpiece material

	Unit	Water (Dielectric Fluid)	Carbide Metal G55
Density ρ	[kg/m^3]	1000	15630
Dynamic viscosity μ	[Pa·s]	$1\cdot10^{-3}$	$4\cdot10^{-3}$
Specific heat capacity c_p	[J/(kg·K)]	4190	400
Thermal conductivity κ	[W/(m·K)]	0.6	70
Latent heat of melting L_f	[J/kg]	-	$1.92\cdot10^5$
Latent heat of vaporization L_v	[J/kg]	-	$4.009\cdot10^6$
Surface tension coefficient ψ	[N/m]	1.9	
Liquidus Temperature T_l	[K]	-	2690
Melting Temperature T_m	[K]	-	2700
Solidus Temperature T_s	[K]	-	2710
Vaporization Temperature T_v	[K]	-	6000

Physics and boundary conditions

The simulations were performed using COMSOL Multiphysics™. The heat transfer module, the laminar two phase flow module and the level-set module were selected to model the crater formation.
Due to the high input of thermal energy from the plasma channel, the temperature of the workpiece material increases over the melting and vaporization temperatures of the workpiece material. This causes a crater formation and a displacement of the interface of the workpiece and the dielectric fluid. To model the resulting geometry deformation and surface topology

the level-set method was used. The level-set method uses a fixed mesh in the whole geometry and is able to track complex changes of the surface geometry. To define the different materials and phases the level-set variable ϕ was set to 1 in the solid phase (workpiece) and 0 in the fluid phase (dielectric fluid). At the initial state, the fluid phase was defined in domain I and the solid phase in domain II. The level-set variable ϕ is equal to 0.5 at the interface and was defined at boundary 7 at the initial state. Near the interface the level-set variable varies smoothly to avoid numerical issues. Figure 3 illustrates the numbering of the domains and boundaries.

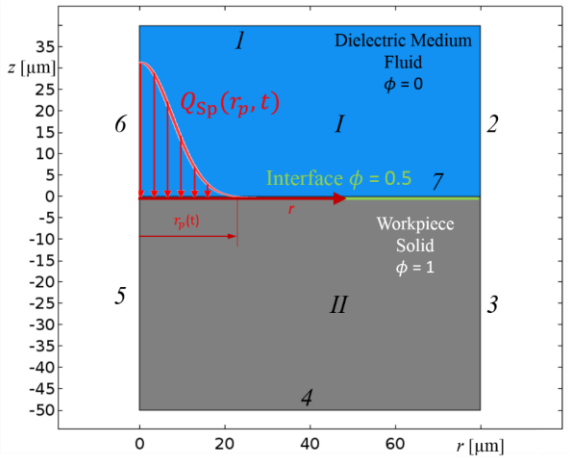

Figure 3. Initial geometry; definition of the level-set variable ϕ and definition of the domain and boundary numbers

The material property definitions also depend on the level-set variable ϕ. The velocity field $\vec{u}$ from the Navier-Stokes equations is used to calculate the movement of the level-set variable. Equation (1) shows the general level-set equation.[15]

$$\frac{\partial \phi}{\partial t} + \vec{u} \cdot \nabla \phi = \gamma \nabla \cdot \left(\varepsilon_{ls} \nabla \phi - \phi(1-\phi) \frac{\nabla \phi}{|\nabla \phi|} \right) \quad (1)$$

Here the variable t is the process time, γ is the reinitialization parameter and ε_{ls} the interface thickness controlling parameter. The reinitialization parameter γ was defined in the range of the expected maximal velocity.

To implement internal boundaries at the interface, the position of the interface has to be determined exactly. Therefore, the delta function of the level-set variable $\delta(\phi)$ was used which attains a value of zero outside the interface and is described by equation (2).[15]

$$\delta(\phi) = 6|\nabla \phi||\phi(1-\phi)| \quad (2)$$

To calculate the velocity field, the conservation of momentum is solved in all phases and is shown in equation (3).

$$\rho(\phi)\frac{\partial \vec{u}}{\partial t} + \rho(\phi)(\vec{u} \cdot \nabla)\vec{u} =$$
$$\nabla \cdot [-\rho(\phi) I + \mu(\phi)(\nabla \vec{u} + (\nabla \vec{u})^{\mathrm{T}})] + F_{\mathrm{St}} + F_{\mathrm{D}} + \rho g \quad (3)$$

Here F_{St} is the surface tension force, I is the identity matrix, F_{D} is an additional damping force, ρ is the density and g the gravity acceleration. The material properties are depend on the level-set variable ϕ. The density and viscosity are defined in equation (4) and (5) and depend on the density of the workpiece ρ_{Wp} and the density of the dielectric fluid ρ_{Df} respectively the viscosity of the workpiece μ_{Wp} and of the viscosity of the dielectric fluid μ_{Df}.

$$\rho(\phi) = \rho_{\mathrm{Wp}} + (\rho_{\mathrm{Df}} - \rho_{\mathrm{Wp}})\phi \quad (4)$$

$$\mu(\phi) = \mu_{\mathrm{Wp}} + (\mu_{\mathrm{Df}} - \mu_{\mathrm{Wp}})\phi \quad (5)$$

The surface tension force is defined in equation (6).[15]

$$F_{\mathrm{St}} = \nabla \cdot (\psi(I - (nn^T))\delta) \quad (6)$$

The surface tension coefficient ψ was assumed as constant. As a result, the Marangoni effect is neglected. The role of the damping force F_{D} is to reduce the velocity of the workpiece material whenever the temperature is below the melting temperature T_{m} and is implemented as a source term. The damping force is calculated by equation (7) and (8). [14–16]

$$F_{\mathrm{D}} = -C\left(\frac{(1-\alpha)^2}{\alpha^3 + \varepsilon}\right) \cdot \vec{u} \quad (7)$$

$$\alpha(T) = \begin{cases} 0 \; for \; T < T_{\mathrm{s}} \\ \frac{T - T_{\mathrm{l}}}{T_{\mathrm{l}} - T_{\mathrm{s}}} \; for \; T_s < T < T_{\mathrm{l}} \\ 1 \; for \; T > T_{\mathrm{l}} \end{cases} \quad (8)$$

Here $\alpha(T)$ is the volume fraction of the liquid phase and considers the transition zone between the solid and liquid phase of the workpiece material. T_{s} is the solidus temperature and T_{l} is the liquidus temperature shown in table 1. C and ε are arbitrary constants. C has to be large and ε very small in order to represent realistic material behavior. Table 2 summarizes the parameters.

Table 2. Parameter to calculate the damping force

Parameter	Unit	Value
C	[kg/m^3·s]	10^6
ε	-	$1 \cdot 10^{-3}$

The conservation of energy is described in equation (9). The variable T represents the temperature, c_p the specific heat capacity and Q_i is the sum of inwards and outwards heat fluxes.

$$\rho c_\mathrm{p} \frac{\partial \boldsymbol{T}}{\partial t} + \rho c_\mathrm{p} \vec{\boldsymbol{u}} \cdot \nabla \boldsymbol{T} = \nabla \cdot [k \nabla \boldsymbol{T}] + Q_\mathrm{i} \quad (9)$$

The specific heat capacity c_p depends on the level-set variable and is shown in equation (10).

$$c_\mathrm{p}(\phi) = c_{\mathrm{p,Wp}}(T) + \left(c_\mathrm{Df} - c_{\mathrm{p,Wp}}(T)\right)\phi \quad (10)$$

Due to the phase change of the workpiece, the latent heat of melting has to be considered. Therefore the specific heat capacity $c_{\mathrm{p,Wp}}$ of the workpiece material was defined corresponding to equation (11) as a function of the temperature including the latent heat of melting L_f by adding a Gaussian distribution focusing the melting temperature T_m.[16]

$$c_{\mathrm{p,Wp}} = c_\mathrm{ps} + L_\mathrm{f} \cdot \frac{e^{-\left(\frac{(T-T_\mathrm{m})^2}{(T_\mathrm{l}-T_\mathrm{s})^2}\right)}}{\sqrt{\pi (T_\mathrm{l}-T_\mathrm{s})^2}} \quad (11)$$

The heat flux Q_i is a sum of the inward heat flux due to the discharge respectively the plasma channel Q_sp.The outwards heat flux Q_v is a consequence of the vaporization phenomena. The definition of the heat flux is shown in equation (12).

$$Q_\mathrm{i} = Q_\mathrm{sp} + Q_\mathrm{v} \quad (12)$$

The inward heat flux due to the discharge is modeled as a heat source which is a function of the electric discharge current I and the electric discharge voltage U. Equation (13) shows the resulting definition of the inward heat flux. [9]

$$Q_\mathrm{sp} = 4.57 \cdot F_\mathrm{c} \cdot I \cdot U \cdot e^{-4.5 \cdot \left[\frac{r}{r_\mathrm{p}}\right]^2} \cdot \delta(\phi) \quad (13)$$

It can be seen that the inward heat is defined as Gaussian distribution in the plasma channel where r is the radial distance from the plasma channel center and r_p the radius of the plasma channel which is defined in equation (14).[17] The definition of the arbitrary constants 4.57 and 4.5 was based on results from different works. [9, 10, 13] The energy distribution factor F_c was set to 0.183. Furthermore, the heat flux equation also depend on the delta function of the level-set variable to locate the inward heat flux at the workpiece surface.

$$r_p = 2.04 \cdot I^{0.43} \cdot {t_\mathrm{e}}^{0.44} \quad (14)$$

Here the parameter t_e is the discharge time. In this work, the discharge voltage was derived by principle current and voltage functions using a static pulse generator. Figure 4 shows the schematic electric current and electric voltage profile. The average discharge voltage $\bar{u}_\mathrm{e}$ and the average discharge current $\bar{\imath}_\mathrm{e}$ are assumed as constant over the discharge time t_e. In this work the assumed discharge voltage U is equal to the average discharge voltage $\bar{u}_\mathrm{e}$ and the discharge current I is equal to the average discharge current $\bar{\imath}_\mathrm{e}$.

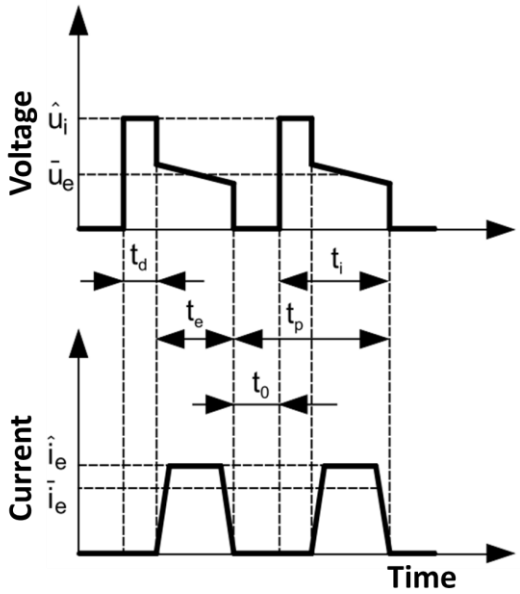

Figure 4. Schematic profile of the electric discharge voltage U and the electric discharge current I of a static pulse generator [18]

The outward heat flux Q_v is an energy loss due to the vaporization of the workpiece material and is represented in equation (15). [16]

$$Q_\mathrm{v} = -L_v \cdot \dot{m}_v(\boldsymbol{T}) \cdot \delta(\phi) \quad (15)$$

The outward heat flux depends on the latent heat of vaporization L_v, the mass flow rate of the vaporization of the workpiece material $\dot{m}_v$ and the delta function of the level-set variable.
The mass flow rate is defined in equation (16) and depends on the temperature and the saturated vapor pressure p_sat which is defined in equation (17).[16]

$$\dot{m}_{\mathrm{v}}(T) = \sqrt{\frac{m}{2\pi k_{\mathrm{b}}}} \cdot \frac{p_{\mathrm{sat}}(T)}{\sqrt{T}} \cdot (1 - \beta_{\mathrm{r}}) \qquad (16)$$

$$p_{\mathrm{sat}}(T) = p_a \cdot e^{\left[\frac{m \cdot L_{\mathrm{v}}}{k_{\mathrm{b}} \cdot T_{\mathrm{v}}}\left(1 - \frac{T_{\mathrm{v}}}{T}\right)\right]} \qquad (17)$$

Here m is the atomic weight of the workpiece material, k_{b} the Boltzmann constant, p_{a} the atmospheric pressure and β_{r} the retrodiffusion coefficient which is zero.
To consider the vaporization phenomena in the velocity field, the continuity equation as well as the level-set equation (1) were modified by adding a source term which is located at the interface. The modified continuity equation is defined in equation (18).

$$\rho \nabla \cdot (u) = \dot{m}_{\mathrm{v}} \delta(\phi) \left(\frac{\rho_{\mathrm{Wp}} - \rho}{\rho^2}\right) \qquad (18)$$

The modified level-set equation is shown in equation (19)

$$\frac{\partial \phi}{\partial t} + \vec{u} \cdot \nabla \phi - \dot{m}_{\mathrm{v}} \delta(\phi) \left(\frac{\phi}{\rho_{\mathrm{Wp}}} - \frac{1 - \phi}{\rho_{\mathrm{Df}}}\right) = \gamma \nabla \cdot \left(\varepsilon_{\mathrm{ls}} \nabla \phi - \phi(1 - \phi) \frac{\nabla \phi}{|\nabla \phi|}\right) \qquad (19)$$

To reduce the numerical effort the simulation was defined as an axial symmetric model. Therefore boundary 5 and 6 were defined as axial symmetry for all physical phenomena. Furthermore a convective heat flux was defined at boundary 1 and 2. Boundary 3 and 4 were defined as thermal insulated. Boundary 1, 2, 3 and 4 were also defined as a no slip wall.

Meshing

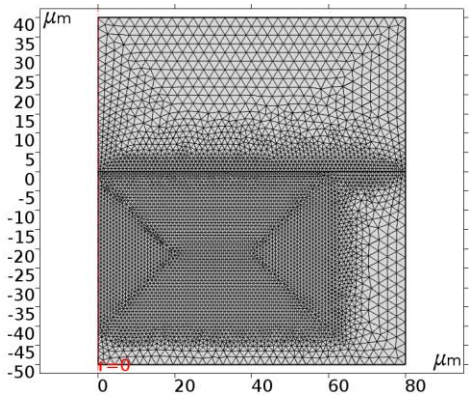

Figure 5. Derived mesh of the geometry

The generated mesh is shown in figure 5. It was defined as a free triangular mesh. The maximum mesh size at the initial interface and in the area where the crater formation is expected, was set to 1 µm. The maximum element-growing rate was defined as 1.05. The entire mesh consists of 10199 elements.

Results single crater formation simulation

Figure 6 shows the crater formation during one single pulse discharge with a discharge energy E_{D} of 3.5 mJ at selected time steps. For clear visualization the dielectric fluid domain is hidden. The false color represents the variable z in µm. It can be seen in figure 6 a) that the surface is completely smooth at the start of the discharge at t = 0 µs. After 5.0 µs, the formation of the single crater takes place and the topology of the workpiece surface changes. With increasing discharge time, the depth h_{c} and the crater radius r_{c} are increasing (figure 6 c)). The resulting shape of the crater in shown figure 6 d).

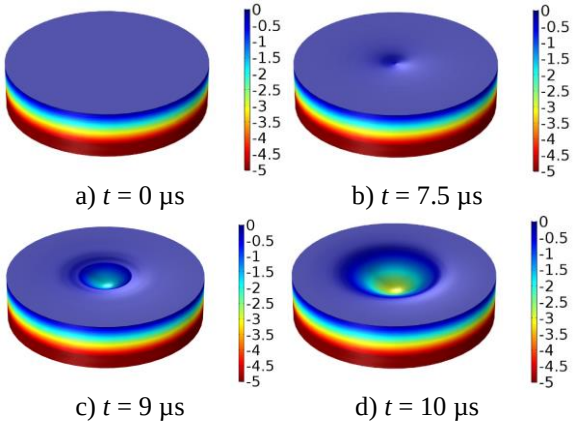

Figure 6. Crater formation due to one single pulse during a discharge time of 10 µs at selected time steps; E_{D} = 3.5 mJ, I = 5 A, U = 70 V, t_{e} = 10 µs; the false color represents the variable z in µm

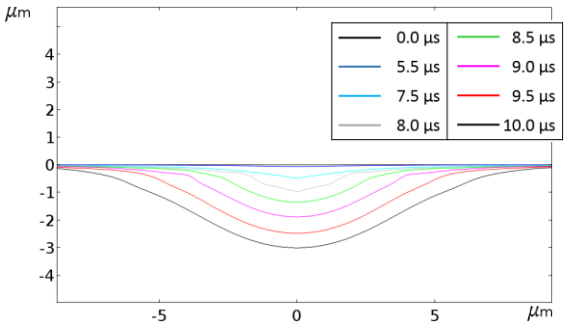

Figure 7. Profile of the crater due to one single discharge pulse during a discharge time of 10 µs at selected time steps; E_{D} = 3.5 mJ, I = 5 A, U = 70 V, t_{e} = 10 µs

Figure 7 shows the profile of the resulting crater as function of the discharge time. It shows that the formation of the crater starts at a discharge time of around 5 µs and subsequently the depth of the crater as well as the radius of the crater increase very fast.

This is a result of the high heat input of the plasma channel. After a discharge time of 10 µs, the resulting depth of the single crater is 3 µm and the resulting radius of the single crater is around 8 µm.
To achieve a workpiece with defined properties, for example a high roughness, it is necessary to vary the machining conditions especially the applied discharge energy. Therefore the electric discharge current I is increased by 50 % while the discharge voltage and discharge time remained unchanged. In consequence, the discharge energy increases. Figure 8 shows the crater formation during one discharge with a discharge energy E_D of 5.25 mJ. In comparison with results with smaller discharge energy it can be seen that the crater depth and radius increases more quickly and a small bulk appears at the edge of the resulting crater, which is a result of the interaction between the pressure due to the phase change and the molten workpiece material.

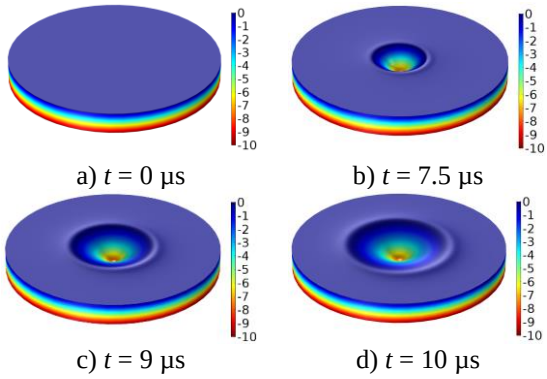

Figure 8. Crater formation due to one single pulse during a discharge time of 10 µs at selected time steps; E_D = 5.25 mJ, I = 5 A, U = 70 V, t_e = 10 µs; the false color represents the variable z in µm

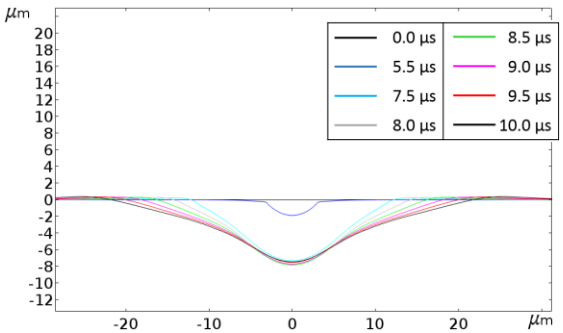

Figure 9. Profile of the crater due to one single discharge pulse during a discharge time of 10 µs at selected time steps; E_D = 5.25 mJ, I = 7,5 A, U = 70 V, t_e = 10 µs

Figure 9 shows the profile of the resulting crater as function of the discharge time. The resulting depth h_c is 7.8 µm at about 9 µs After reaching this time the expansion of the crater stops. This is a result of the increasing heat outflow of the workpiece due to the expansion of the surface area and the following outward heat flux due to vaporization and conduction which is higher than the inward heat flux due to the plasma channel. The resulting radius of the single crater r_c is 22 µm. The profile of the single crater with a higher discharge energy is distinguished from the profile with small discharge energy because of the different size of the plasma channel and the different Gaussian distribution of the heat input.

Calculation of the surface topography by single crater superimposition

There are a few approaches known for laser as well as for EDM processes for the calculation of the surface microstructure or roughness, respectively. Yasa and Kruth developed a model based on the kinematics of laser processing with the aim to evaluate local energy input and ablation depth. However, in this model three-dimensional ablation geometries were not considered so far [19]. Izquierdo presented a model for EDM processing considering the effect of multiple discharges by using a calculated temperature distribution in combination with a discharge probability function. By the help of an expensive model calibration, simulations showed accurate results [20].
In the area of machining processes, material removal is often described by the intersection of a geometrically defined tool with a workpiece. Figure 9 shows the principle of this geometric approach. Aim of the present study is to adapt this principle to the EDM process for predicting the surface structure on the microscopic scale by the help of simulated crater formations.

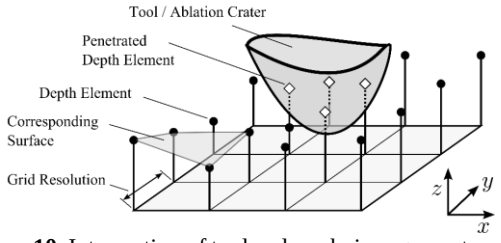

Figure 10. Intersection of tool and workpiece geometry with dexel model for surface representation, adopted from [21]

Depending on the complexity of the workpiece, different models for the geometry description were described [22]. For flat surfaces, the so called dexel (depth element) model is a common model, because the workpiece surface can be described numerically by using arrays or matrices with the values corresponding to the element height of the surface structure. Figure 10 shows the principle of the dexel model.

For the simulation of the surface formation during the EDM process the approach of intersecting tool and workpiece was adapted to the EDM process by subtracting the crater geometry several times and at different positions from the workpiece surface. This principle was assessed suitable due to the perception that only one discharge occurs at a specific point of time in real EDM processes. Because of the microscopic scale and the advantages concerning the computational effort, a dexel model was preferred for surface representation in this study.
In real processes, the ablation of material does not occur on ideal flat workpiece surfaces but rather on rough surface conditions. In order to consider the initial state of the surface in the area of ablation, a weight function describing the local intensity of the ablation compared to the flat reference case was introduced:

$$Z_{\mathrm{wp}}(n+1) = Z_{\mathrm{wp}}(n) - W_{\mathrm{ablation}} \cdot Z_{\mathrm{ref}}(r) \quad (19)$$

In this equation, Z_{wp} denotes the surface geometry in z-direction, W_{ablation} the ablation weights and Z_{ref} the depth of the reference crater as a function of the radius r. The ablation weights are calculated from the weight function that characterizes the effect of the initial state of a surface structure on the ablation depth or intensity of an EDM discharge, respectively. The ablation weights are determined based on the weight function. Their values are calculated in every simulation step for every point of the surface in the area of ablation and depend thereby on the radius r as well as on the initial height difference Δh between the regarded point on the surface to the center of the crater which is shown in figure 11.

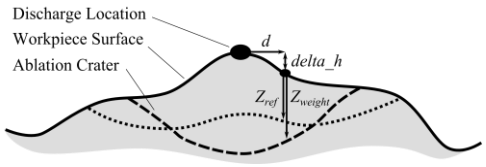

Figure 11. Consideration of non-flat surfaces by locally weighted ablation depth

For the specification of the weight function W, Multiphysics Simulations with COMSOL using the presented model were carried out. For this purpose, the initial domain of the solid phase (see Figure 3, domain II) was shaped conically with the center as the highest located point. Based on the results of these simulations, the weight function W could be derived by the help of equation (20):

$$W(r, \Delta h) = Z_{\mathrm{weight,sim}}(r, \Delta h) / Z_{\mathrm{ref}}(r) \quad (20)$$

In this context, $Z_{\mathrm{weight,sim}}$ denotes the simulated crater geometry measured from the initial surface. During EDM, local conduction and melting of material occurs at the point with maximum electric potential between workpiece and electrode. In the EDM model the position of crater formation was assigned as the minimal distance from the workpiece to a flat counter surface in each case. A random distribution of the craters at the beginning of the simulations was ensured by initializing the surface geometry with a very small random roughness.
The algorithm realizing the crater superimposition was implemented in MATLAB. Necessary information was transferred to the workspace by the help of the MATLAB LiveLink™ Application.

Resulting surface topography

For the simulations, a workpiece with a length of 150 µm and a width of 150 µm with a grid resolution of 1 µm was applied. The number of discharges was set to a value, at which the surface roughness, characterized by the parameter *Sa* [22] became stationary.

a) Superimposition of 100 single craters

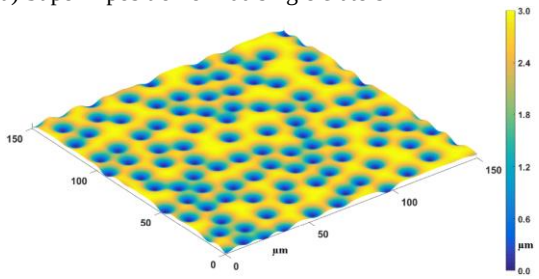

b) Superimposition of 300 single craters

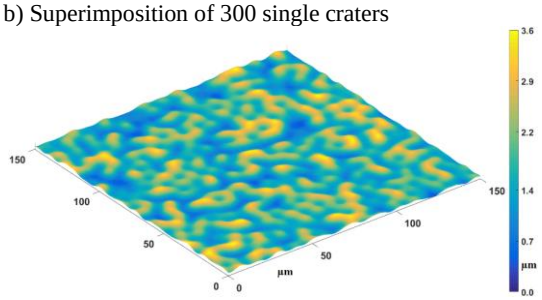

c) Superimposition of 1000 single craters

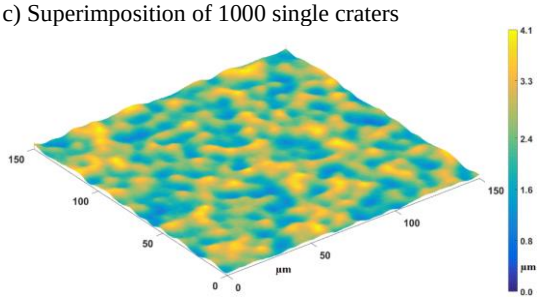

Figure 12. Resulting surface of the workpiece for different number of superimposed single discharge craters, E_{D} = 3.5 mJ

Figure 12 shows results for multiple stages of ablation with superimposed craters. Figure 12 a) shows the resulting surface after 100 discharges. In figure 12 b) the result for 300 single discharges can be seen. The roughness of the surfaces increases compared to the first case. Figure 12 c) represents the final surface for 1000 discharges. Single crater geometries are not observable which is a result of the high number of superimposed discharges. In the stationary case, a mean surface roughness of Sa = (0.54 ± 0.01) µm was obtained in 10 simulation runs.
Figure 13 shows corresponding results obtained with the higher pulse energy of 5.25 mJ. In this case, a surface roughness of Sa = (1.25 ± 0.10) µm could be determined finally. An in-depth comparison between simulation results and surface measurements will be subject of future work.

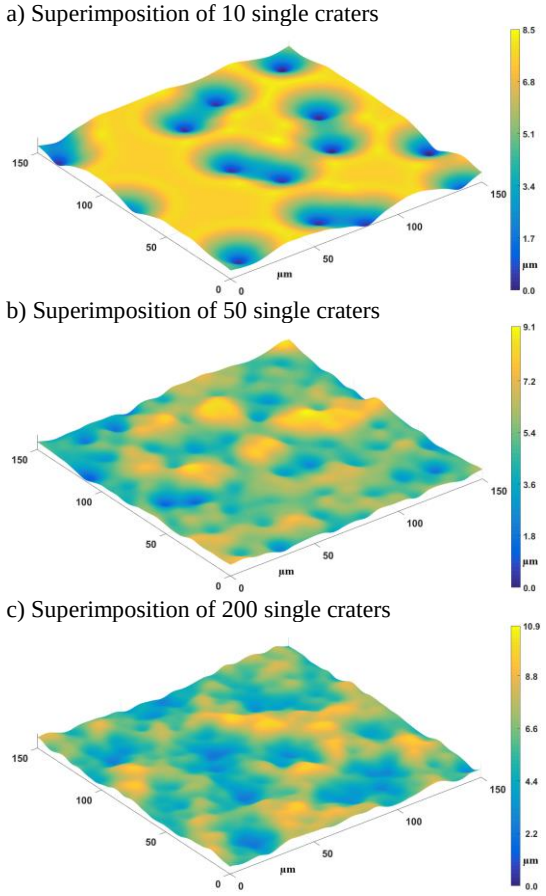

Figure 13. Resulting surface of the workpiece for different number of superimposed single discharge craters, E_D = 5.25 mJ

Summary

In this study an approach for the simulation of crater formation during a single electrical discharge was described. The material ablation was defined by the help of modelling the vaporization phenomena which introduces a pressure as a result of the phase change of the workpiece material from solid respectively liquid phase to vapor phase. To simulate the discharge plasma, an additional heat source was implemented which occurs directly at the workpiece surface. To track the interface due to the crater formation, the level-set method was used. Different electrical discharge conditions were considered and analyzed to evaluate the influence of the input process parameter on the resulting crater shape. Based on the resulting crater shape, a method to calculate the surface formation by help of superimposition was described. With this approach, it is possible to study the influence of the discharge conditions and the initial surface structure on the topography of the machined surface. Especially the prediction of resulting surface roughness using this simulation method is relevant for the design of the electrical discharge conditions. Next steps are the implementation of experimental electric discharge voltage and electric discharge current functions and the model validation with single discharge experiments. Furthermore a comparison with measurements of electrical discharge machined surfaces will be necessary.

Acknowledgements

This project is funded by the Federal Ministry of Economics and Technology, following a decision of the German Bundestag.

References

[1] A. Schubert, H. Zeidler, M. H. Oschätzchen, J. Schneider, and M. Hahn, “Enhancing Micro-EDM using Ultrasonic Vibration and Approaches for Machining of Nonconducting Ceramics,” *Strojniški Vestn. – J. Mech. Eng.*, vol. 59, no. 3, pp. 156–164, 2013, ISSN: 00392480, DOI:10.5545/sv-jme.2012.442

[2] M. Hackert-Oschätzchen, M. Kreißig, M. Kowalick, H. Zeidler, A. Schubert, O. Kröning, M. Herzig, and H.-P. Schulze, “Single discharge simulations of needle pulses for electrothermal ablation,” *Proc. Eur. COMSOL Conf.*, pp. 1–3, 2013

[3] D. D. DiBitonto, P. T. Eubank, M. R. Patel, and M. A. Barrufet, “Theoretical models of the electrical discharge machining process. I. A simple cathode erosion model,” *J. Appl. Phys.*, vol. 66, no. 9, pp. 4095–4103, 1989, ISBN: http://dx.doi.org/10.1063/1.343994, ISSN: 00218979, DOI:10.1063/1.343994

[4] P. Taylor, B. Bozkurt, A. M. Gadalla, and P. T. Eubank, “Materials and Manufacturing Processes Simulation of Erosions in a Single Discharge EDM Process Simulation of E ~ rosions in a Single Discharge EDM Process,” *Mater. Manuf. Process.*, pp. 555–563, 1996

[5] S. Das, M. Klotz, and F. Klocke, “EDM simulation: Finite element-based calculation of deformation, microstructure and residual stresses,” *J. Mater. Process. Technol.*, vol. 142, no. 2, pp. 434–451, 2003, ISBN: 4902418027401, ISSN: 09240136, DOI:10.1016/S0924-0136(03)00624-1

[6] B. Shao and K. P. Rajurkar, “Modelling of the crater formation in micro-EDM,” *Procedia CIRP*, vol. 33, pp. 376–381, 2015, ISSN: 22128271, DOI:10.1016/j.procir.2015.06.085

[7] L. Liqing, G. Chenhao, and S. Yingjie, “Simulation Analysis of the Crater Size for Single-pulse Dry Electrical Discharge Machining,” *Procedia CIRP*, vol. 68, pp. 292–297, 2018, ISBN: 0000000329, ISSN: 22128271, DOI:10.1016/j.procir.2017.12.066

[8] Y. B. Guo, A. Klink, and F. Klocke, “Multiscale modeling of sinking-EDM with Gaussian heat flux via user subroutine,” *Procedia CIRP*, vol. 6, pp. 438–443, 2013, ISSN: 22128271, DOI:10.1016/j.procir.2013.03.047

[9] S. N. Joshi and S. S. Pande, “Thermo-physical modeling of die-sinking EDM process,” *J. Manuf. Process.*, vol. 12, no. 1, pp. 45–56, 2010, ISSN: 15266125, DOI:10.1016/j.jmapro.2010.02.001

[10] H. R. Fazli Shahri, R. Mahdavinejad, M. Ashjaee, and A. Abdullah, “A comparative investigation on temperature distribution in electric discharge machining process through analytical, numerical and experimental methods,” *Int. J. Mach. Tools Manuf.*, vol. 114, no. August 2016, pp. 35–53, 2017, ISSN: 08906955, DOI:10.1016/j.ijmachtools.2016.12.005

[11] A. Mishra, S. Bhattacharya, D. D. S. Kr, and G. K. Dey, “Multiphysics Based Electrical Discharge Machining Simulation,” *COMSOL Conf. 2015 Pune*, vol. 3, no. 2010, p. 2015, 2015

[12] E. Weingärtner, F. Kuster, and K. Wegener, “Modeling and simulation of electrical discharge machining,” *Procedia CIRP*, vol. 2, no. 1, pp. 74–78, 2012, ISSN: 22128271, DOI:10.1016/j.procir.2012.05.043

[13] J. Tang and X. Yang, “A novel thermo-hydraulic coupling model to investigate the crater formation in electrical discharge machining,” *J. Phys. D. Appl. Phys.*, vol. 50, no. 36, 2017, ISSN: 13616463, DOI:10.1088/1361-6463/aa7bb7

[14] J. Tao, J. Ni, and A. J. Shih, “Modeling of the Anode Crater Formation in Electrical Discharge Machining,” *J. Manuf. Sci. Eng.*, vol. 134, no. 1, p. 011002, 2012, ISBN: 1087-1357, ISSN: 10871357, DOI:10.1115/1.4005303

[15] Comsol, “CFD Module User ’ s Guide,” 2015, ISBN: 1781273332

[16] M. Courtois, M. Carin, P. Le Masson, S. Gaied, and M. Balabane, “A complete model of keyhole and melt pool dynamics to analyze instabilities and collapse during laser welding,” *J. Laser Appl.*, vol. 26, no. 4, p. 042001, 2014, ISBN: 0277-786X, ISSN: 1042-346X, DOI:10.2351/1.4886835

[17] M. Shabgard, R. Ahmadi, M. Seyedzavvar, and S. N. B. Oliaei, “Mathematical and numerical modeling of the effect of input-parameters on the flushing efficiency of plasma channel in EDM process,” *Int. J. Mach. Tools Manuf.*, vol. 65, pp. 79–87, 2013, ISBN: 0890-6955, ISSN: 08906955, DOI:10.1016/j.ijmachtools.2012.10.004

[18] F. Klocke and W. König, *Fertigungsverfahren 3; Abtragen, Generieren und Lasermaterialbearbeitung*. Berlin: Springer-Verlag, 2007, ISBN: 978-3-540-48954-2

[19] E. Yasa and J. P. Kruth, “Investigation of laser and process parameters for Selective Laser Erosion,” *Precis. Eng.*, vol. 34, no. 1, pp. 101–112, 2010, ISBN: 0141-6359, ISSN: 01416359, DOI:10.1016/j.precisioneng.2009.04.001

[20] B. Izquierdo, J. a. Sánchez, S. Plaza, I. Pombo, and N. Ortega, “A numerical model of the EDM process considering the effect of multiple discharges,” *Int. J. Mach. Tools Manuf.*, vol. 49, no. 3–4, pp. 220–229, 2009, ISSN: 08906955, DOI:10.1016/j.ijmachtools.2008.11.003

[21] R. Zhang, P. Steinert, and A. Schubert, “Microstructuring of surfaces by two-stage vibration-assisted turning,” *Procedia CIRP*, vol. 14, pp. 136–141, 2014, ISSN: 22128271, DOI:10.1016/j.procir.2014.03.026

[22] B. Denkena and H. K. Tönshoff, *Spanen*. Berlin, Heidelberg: Springer Berlin Heidelberg, 2011, ISBN: 978-3-642-19771-0, DOI: 10.1007/978-3-642-19772-7